Lab on a Chip

PAPER

View Article Online
View Journal | View Issue

Cite this: *Lab Chip*, 2025, **25**, 613

Microfluidic vessel-on-chip platform for investigation of cellular defects in venous malformations and responses to various shear stress and flow conditions†

Mohammadhassan Ansarizadeh,‡[a] Hoang-Tuan Nguyen, ‡[ab] Bojana Lazovic,[acd] Jere Kettunen,[b] Laknee De Silva,[a] Ragul Sivakumar,[b] Pauliina Junttila,[b] Siiri-Liisa Rissanen,[b] Ryan Hicks,[cde] Prateek Singh[b] and Lauri Eklund*[a]

A novel microfluidic platform was designed to study the cellular architecture of endothelial cells (ECs) in an environment replicating the 3D organization and flow of blood vessels. In particular, the platform was constructed to investigate EC defects in slow-flow venous malformations (VMs) under varying shear stress and flow conditions. The platform featured a standard microtiter plate footprint containing 32 microfluidic units capable of replicating wall shear stress (WSS) in normal veins and enabling precise control of shear stress and flow directionality without the need for complex pumping systems. Using genetically engineered human umbilical vein endothelial cells (HUVECs) and induced pluripotent stem cell (iPSC)-derived ECs (iECs) to express the recurrent *TIE2*^{L914F} VM mutation we assessed responses on EC orientation and area, actin organization, and Golgi polarization to uni- and bidirectional flow and varying WSS. Comparison of control and *TIE2*^{L914F} expressing ECs showed differential cellular responses to flow and WSS in terms of cell shape elongation, orientation of F-actin, and Golgi polarization, indicating altered mechanosensory or mechanotransduction signaling pathways in the presence of the VM causative mutation. The data also revealed significant differences in how the primary and iPSC-derived iECs responded to flow. As a conclusion, the developed microfluidic platform allowed simulation of multiple flow conditions in a scalable and pumpless format. The design made it a desirable tool for studying different EC types as well as cellular changes in vascular disease. The platform should offer new opportunities for biomechanical research by providing a controlled environment to analyze the flow-dependent mechanosensory pathways in ECs.

Received 30th September 2024,
Accepted 6th January 2025

DOI: 10.1039/d4lc00824c

rsc.li/loc

Introduction

In blood vessels, endothelial cells (ECs) constantly experience wall shear stress (WSS) from blood flow, which is a critical factor regulating EC processes such as proliferation, migration, and gene expression.[1,2] The magnitude and direction of shear stress vary significantly between arteries, veins, and capillaries, dictating EC morphology, function, and vascular health.[1,3–6] Changes in the vascular cells and in the shape and physical properties of blood vessels affect blood flow (and *vice versa*) and may lead to vascular remodeling in normal development and in cardiovascular diseases.[6] Because of the shortage of suitable models to mimic shape and flow, their roles in vascular pathophysiology have often been ignored. With the advancement in microfabrication and microtechnology, it is now possible to fabricate and simulate blood-flow within microchannels.[7–9] As a result, a significant volume of research about on-chip 3D vasculature networks capable of mimicking physiological and disease conditions has been reported in the recent past aimed at studying, *e.g.* thrombosis, stenosis, and vascularized epithelial barriers.[8,10–13] Most of these systems, however, are pump-based, which introduces several challenges including the requirement for extensive tubing, the complexity of operation, the consumption of large volumes of medium and

[a] *Oulu Center for Cell-Matrix Research, Biocenter Oulu and Faculty of Biochemistry and Molecular Medicine, University of Oulu, P.O. Box 5000, FI-90014 Oulu, Finland. E-mail: lauri.eklund@oulu.fi; Tel: +358 50 350 1782*
[b] *Finnadvance Ltd., Oulu, Finland*
[c] *BioPharmaceuticals R&D Cell Therapy Department, Research and Early Development, Cardiovascular, Renal, and Metabolism (CVRM), BioPharmaceuticals R&D, AstraZeneca, Gothenburg, Sweden*
[d] *Translational Genomics, Discovery Sciences, BioPharmaceuticals R&D, AstraZeneca, Gothenburg, Sweden*
[e] *School of Cardiovascular and Metabolic Medicine & Sciences, King's College London, London, UK*
† Electronic supplementary information (ESI) available. See DOI: https://doi.org/10.1039/d4lc00824c
‡ These authors equally contributed to this study.

investigational substances, such as drug candidates.[14–18] Gravity-driven microfluidic chip systems have advantages due to their simplicity and scalability; however, most models are limited to bidirectional flow, thus failing to accurately mimic physiological conditions.[19–22] Efforts to design pumpless unidirectional flow systems for vascular studies have faced challenges due to high complexity, fabrication difficulties, and limited versatility.[23–25]

Venous malformations (VMs) are developmental defects in vascular morphogenesis characterized by abnormally enlarged vein-like channels resulting in low or stagnant blood flow.[26–30] The role of abnormal flow in VM pathogenesis is currently unknown and there has been no study to create microfluidic-based models for VMs. Gain-of-function mutations in the EC receptor tyrosine kinase *TIE2* are identified in more than 50% of VMs and the L914F amino acid substitution is found to be the most common sporadic VM mutation.[31] Furthermore, somatic activating mutations in *PIK3CA* are found in the majority of *TIE2* mutation-negative VMs.[29,32,33] These genetic findings indicate the importance of TIE2-PI3K signaling in the VM pathogenesis; however, the underlying cellular mechanisms downstream from mutated TIE2-PI3K are not completely understood.

Standard treatment of VMs is based on surgical resection and sclerotherapy, and symptoms can be relieved by compression or thrombosis treatment.[34–36] These treatments, however, are not curative and can be ineffective due to the size, location, number or invasiveness of VM lesions. Current microfluidic models fail to adequately simulate the slow flow dynamics and the pathological shear stress levels seen in VMs, which are crucial for studying the endothelial dysfunction in these conditions. Furthermore, in addition to the *TIE2* mutation positive VMs, the causal relationship between flow and lesion formation in other slow-flow vascular malformations affecting capillaries and lymphatics remains poorly understood due to the lack of suitable models. All in all, for better understanding of disease mechanisms and for the development of evidence-based therapies, there is a need for biologically relevant disease models that replicate the characteristics of pathological flow.

Our research tackled limitations in the current vessel-on-chip models and VM research by introducing an innovative microfluidic design that leverages the gravity-driven, pumpless setup to modulate WSS in both uni- and bidirectional flows. This innovative approach eliminates the need for external pumps and complex tubing, simplifying operation and enhancing scalability. The design was fine-tuned for specific venous WSS ranges, making it ideal for studying VM pathologies. Employing a dual *in vitro* and *in silico* strategy, our platform simulates mechanical stimuli and their effects on both healthy and mutated ECs. It enables detailed studies of the cellular responses of normal and $TIE2^{L914F}$ mutant expressing ECs to varied flow directions and WSS magnitudes. Insights gained from this research illuminated cellular responses in VMs and should help to lead to the identification of new therapeutic targets. In addition to VMs, by focusing on flow directionality and WSS, our platform also offers a valuable novel tool for EC biology.

Materials and methods

Microfluidic vessel-on-chip design and fabrication

Following the American National Standards Institute/Society for Laboratory Automation and Screening (ANSI/SLAS) format, the microfluidic platform consists of 32 microfluidic units for modeling blood vessels. Each unit has a microchannel with varying cross-sectional diameters and a bypass reservoir design to rectify the flow direction through the channel in one way. The microfluidic design, coupled with a fully programmable rocker, overcomes the limitations of current organ-on-a-chip platforms, eliminating the need for complex pumping systems. An important aspect when designing the microfluidic channels is taking into account their flow resistances. The flow rate is a linear function of the applied pressure and is limited by the hydraulic resistance of the microfluidic channel. The hydraulic resistance of channels with rectangular cross sections, typical in microfluidics, can be calculated using the following formula:

$$R = \frac{1}{1 - 0.63\frac{h}{w}} \times \frac{12\mu L}{h^3 w} \quad (1)$$

where L is the length of the microchannel, h and w are the microchannel height and width, respectively, and μ is the dynamic viscosity of the liquid passing through the microchannel, which is cell culture medium. Table 1 presents the detailed dimensions and calculated hydraulic resistance of each microchannel section.

The construction of the microfluidic plate includes two main components, the microchannel layer and the reservoir complex on top; together they form a thick 3D structure within the plate. To replicate the plate, a two-part mold was designed using Solidwork (Dassault Systèmes) and 3D-printed using clear resin on a Form3 stereolithography (SLA) 3D printer (Formlabs). A polydimethylsiloxane (PDMS) kit, RTV615 (Techsil), including the base and the curing agent, were mixed in a ratio of 10 : 1 (by weight) and degassed under vacuum pressure to remove air bubbles before injecting into the 3D printed mold through an electric syringe pump for precise control of flow rate to avoid air bubbles from being trapped. The mold was left for the heat treatment of the PDMS polymer at 65 °C for 4 hours to harden into a transparent solid. Once the PDMS had hardened, it was peeled off from the mold, thus replicating the 3D printed features present on the mold surface. The PDMS replica was

Table 1 Microchannel dimensions and properties

Zone	Length (μm)	Width (μm)	Height (μm)	Hydraulic resistance (Pa s m^{-3})
A	3000	600	200	9.49×10^9
B	3000	400	200	1.64×10^{10}
C	3000	200	200	6.08×10^{10}

then bonded to a thin PDMS film using plasma treatment (Harrick Plasma).

Computational fluidic dynamic studies

To confirm the calculated geometrical designs and flows, COMSOL Multiphysics (COMSOL, Inc.) was used to numerically simulate the hydrodynamic changes in microchannels. The 3D model of a single microfluidic unit was designed in SolidWorks software and exported as a STEP file to import to COMSOL. The laminar flow simulation was defined by the 3D geometry of the microfluidic unit. The gravity vector was set to be determined by the horizontal and vertical components of the microfluidic channel when tilted. A no-slip boundary condition was applied at the walls, laminar inflow with inlet pressure difference according to the Poiseuille equation, and zero outlet pressure with suppressed backflow was selected. The parameters such as gravity acceleration 9.81 m s^{-2}, dynamic viscosity 0.861 × 10^{-3} Pa s, and fluid density 1002 kg m^{-3} were applied according to the fluid properties of DMEM cell culture medium at 37 °C.[37] Wall shear stress (WSS) at the bottom surface of the microchannel along the microchannel length was analyzed and mapped using both colour distribution and 1D plot.

Volume flow measurement

The flow rate in the chip was measured by collecting the volume turnover from the outlet reservoir at different timepoints. First the microchannels were coated with 100 μg mL^{-1} fibronectin and then prefilled with endothelial cell growth medium 2 (EGM2; Gibco, C-22011) supplemented with 10% fetal bovine serum (FBS, Sciencell, 0010), manufacturer supplement mix solution (PromoCell GMbH, C-39215), and 1% penicillin/streptomycin (P/S; Sigma-Aldrich) cell culture medium to replicate the real cell culture condition. The plate with prefilled microchannels was placed on the rocker, tilted at 30°. For each microfluidic unit, ensuring that the inlet and outlet reservoirs were empty, at time point t = 0 s, the upper inlet reservoir was filled with 150 μL EGM2 medium. Hydrostatic pressure difference started to drive the liquid into the outlet reservoir at the lower level. Except for the coating, all the above steps were repeated for various dwell times so that the turnover medium is collected at different timepoints from 0 to 240 s. For every sampling time t, the collected volume V_t yields a flow rate value of $Q_t = (V_t - V_{t-1})/(t - (t - 1))$. The measurements were done at room temperature (RT) on three separate microfluidic units and repeated three times.

Endothelial cell line generation and cultivation

HUVECs were purchased from PromoCell (pooled donor, C-12203) and cultured on attachment factor-coated plates (Cell Applications, 123-500) in EGM2 supplemented with 10% FBS (Sciencell, 0010), with manufacturer supplement mix solution (PromoCell GMbH, C-39215), and 1% P/S. Retroviruses to express bicistronic GFP and TIE2 were generated in 293-GPG-VSV-G packaging cells using pMXs-IRES-GFP vectors.[29] Transduced HUVECs were isolated using fluorescence-activated cell sorting (FACS) based on GFP expression and validated through western blot (Fig. S1†). iECs (WT, OdinCas9-hiPSCs and *TIE2*^{L914F}-hiPSCs) were generated as described previously[21] and verified using western blot (Fig. S1†). The generated HUVECs (HUVEC^{GFP}, *TIE2*^{WT} HUVEC^{GFP}, and *TIE2*^{L914F} HUVEC^{GFP}) were cultured in EGM2 and iECs (*TIE2*^{WT} iECs and *TIE2*^{L914F} iECs) in modETV2 medium.[21] Initially, culture plates were coated with an Attachment Factor Solution (Cell Applications) for 1 h, and then the coating was aspirated without washing. Subsequently, HUVECs and iECs were cultured on coated plates and maintained at +37 °C with 5% CO_2 until reaching full confluency.

Cell culture on chip

On day-1 of the experiment (one day prior to cell loading on chip), the microfluidic channels of the plates were coated with 100 μL of 100 μg mL^{-1} human fibronectin (Corning, 354008) diluted in phosphate-buffered saline (PBS, Gibco, 10010023). The coating solution was incubated for 4 h at +37 °C, 5% CO_2, following an overnight incubation at +4 °C. On day 0 of the experiment, HUVECs and iECs grown to full confluency in a 10 cm plate were trypsinized and suspended in EGM2 cell culture medium. 50 μL suspensions of each EC line with a concentration of 2 × 10^6 cells mL^{-1} were perfused through each channel and incubated in an incubator at 37 °C, 5% CO_2 under static conditions for 4 h following a wash with fresh medium to remove the non-adhered cells. The plates were then kept static in the incubator overnight to allow the cells to fully adhere to the microchannel walls. On day 1, the plates were then placed on two rockers with different programs for uni- or bidirectional flow culture. The medium was changed every 24 h. EGM2 and modETV2 medium were used for HUVECs and iECs, respectively. The cells were under dynamic culture on the chips until day 5.

Immunostaining and confocal microscopy

After conducting experiments for five days, the microfluidic plates were fixed with 4% paraformaldehyde (PFA) for 1 h and then underwent 3 × 5 min washes with PBST (PBS with 0.1% Tween 20). Then, the samples were subjected to simultaneous blocking and staining with primary antibodies in 3% BSA–PBST overnight at +4 °C on a rocker to ascertain that the antibodies were well distributed across the whole channel. The next day the channels were washed 3 × 5 min on the rocker at RT. Similarly, secondary antibody dilutions were prepared in blocking buffer and incubated for 2 h at RT. The stained cells were washed 3 × 5 min with PBST after the secondary antibody incubation. Reagents used were DAPI (Sigma-Aldrich), GM130 (BD Pharmingen, 610822), VE-cadherin (Cell Signaling Technology, 2500), phalloidin-TRITC (R&D Systems, 5783), Alexa Fluor 647-conjugated donkey anti-rabbit IgG (Abcam, ab150113), Alexa Fluor 488 conjugated donkey anti-rabbit IgG (Jackson ImmunoResearch, 711-545-152), Alexa Fluor 488 AffiniPure goat anti-mouse IgG (Jackson ImmunoResearch, 115-545-003), and Alexa Fluor 647

AffiniPure goat anti-mouse IgG (Jackson ImmunoResearch, 115-605-003). The fixed and stained microfluidic units were imaged using a Leica STELLARIS 8 DIVE multiphoton confocal microscope with a spectral fluorescence detector (3 HyD S). 20×/0.75 HC PL APO CS2 air objective and 40×/1.25 HC PL APO motCORR glycerol objective were used, with lasers providing excitation at 405 nm, 488 nm, 561 nm, and 638 nm.

Image analysis

The image processing and analysis were conducted using FIJI a distribution of ImageJ.[38] Cellpose 2.0[39] was utilized to generate general segmentation models for the images acquired. The models were trained manually on approximately 20% of total images, each with a mix of all cell types. The training used VE-Cad staining as a cell segmentation channel and nuclei channel as a reference point. The produced regions of interest (ROIs) were gathered into a single file using a custom script and transferred into FIJI to be analyzed with the inbuilt measurement tools after cleaning up artifacts (*i.e.* empty rows) in the files. Measurements were set to area, shape descriptors and fit ellipse in the 'set measurements menu' of FIJI to acquire datasets containing area, orientation, and shape indicators that were then semi-automatically gathered for analysis. The F-actin analysis was performed on the phalloidin-stained images using the FilamentSensor 2.0 tool[40] using the built-in settings to calculate the dimensions and orientation angle of actin filaments. The analysis of Golgi and nucleus polarization was done using the Polarity-JaM tool.[41] The tool incorporated Cellpose 2.0 for cell ROI segmentation. Within each ROI, the centers of mass for the nucleus and Golgi apparatus were identified. The polarization angle was defined as the angle between the line connecting these two points and the horizontal axis.

Statistical analysis

All statistical analyses were carried out using GraphPad Prism 9 software (Dotmatics). Two-way ANOVA and Tukey's multiple comparison method was used for comparison between groups. Statistical significance is demonstrated in figures by: $*P < 0.05$, $**P < 0.01$, $***P < 0.001$, and $****P < 0.0001$.

Results and discussion

Design, operation, and construction of the microfluidic plate

To mimic blood vasculature precisely, physiological flow rates and shear stress needed to be considered.[1] In a microchannel, the velocity of a fluid at a stationary boundary is zero, yielding the no-slip condition; hence the ECs that line the microvessel walls are under the effects of WSS.[42] To investigate the effects of WSS on the morphology and alignment of ECs, we designed the pumpless microfluidic plate comprising 32 individual microchannels with the footprint of a 96-well plate. Each symmetrical microchannel represents a single vessel with three channel width variations, named as A, B, and C, representing low, medium, and higher shear stress (Fig. 1a). In this design, the fluid flow through the stepwise narrowed regions of the microchannels generates a WSS gradient, which is expected to result in differential responses in EC morphology and orientation. On top of each channel, there is an asymmetrical reservoir complex with an inlet and outlet connecting each channel's end (Fig. 1a). The reservoirs drive the medium for perfusing the microchannels in one way and bypass the medium in the opposite way according to the tilting angle and direction to induce the unidirectional gravity-driven microfluidic flow in the system. The medium in the inlet reservoir is set to be at a higher level (by tilting left at 30°) than the outlet to force fluid flow in only one direction. When the level of liquid in the inlet and outlet starts to equilibrate, the height difference is re-established by quickly changing the tilting direction from the left to 45° on the right to bypass the medium back to the inlet side from the outlet reservoir and reversing the tilt direction to the left to maintain desired unidirectional flow conditions (Fig. 1b). For comparison, the tilting program of the rocker was slightly modified to induce bidirectional flow through the microchannel. When the plate is tilted to the right, the tilting angle is adjusted to be only 30° to avoid medium passing *via* the bypass bridge. During the bypass, the amount of liquid passing the microchannels within 2 s dwelling time can be considered to be negligible. Table 2 shows the detailed settings of the rocker to generate different flow profiles in the microchannels.

While gravity-driven microfluidic systems are a common approach in vessel-on-chip research, especially unidirectional flow systems with bypass structures,[23,24,43] our pumpless design offers distinct advantages in terms of efficiency, simplicity, and versatility. Unlike existing models that are designed for bioprinting, hydrogels[24] or complex fabrication processes,[25] our gel-free system eliminates the need for stabilizing materials, ensuring direct fluid interaction and simplifying both fabrication and operation. Furthermore, previous systems allow only for single operation mode, while our optimized bypass structure allows for both uni- and bidirectional flow. The design also minimizes backflow and expedites medium recirculation, providing consistent and reliable unidirectional flow. By combining ease of use with precise flow control, this streamlined design facilitates high-throughput experimentation, enhances reproducibility, and allows for seamless integration into standard laboratory workflows.

The plate was designed with a scalable production mindset to further meet industry-standard manufacturing method in the future. To fabricate the plate, a hybrid process of liquid silicone injection molding and additive manufacturing was employed as described in previous work.[44] As depicted in Fig. 1c, the injection mold tooling was made by SLA 3D printing to create a 2-part mold setup. The top part of the mold contains the negative 3D structure of the reservoirs while the bottom counterpart consists of the negative 3D microchannel structures. The mold then underwent a post-processing procedure including 96% ethanol washing and UV curing to remove uncured resin residues. Importantly, we discovered that

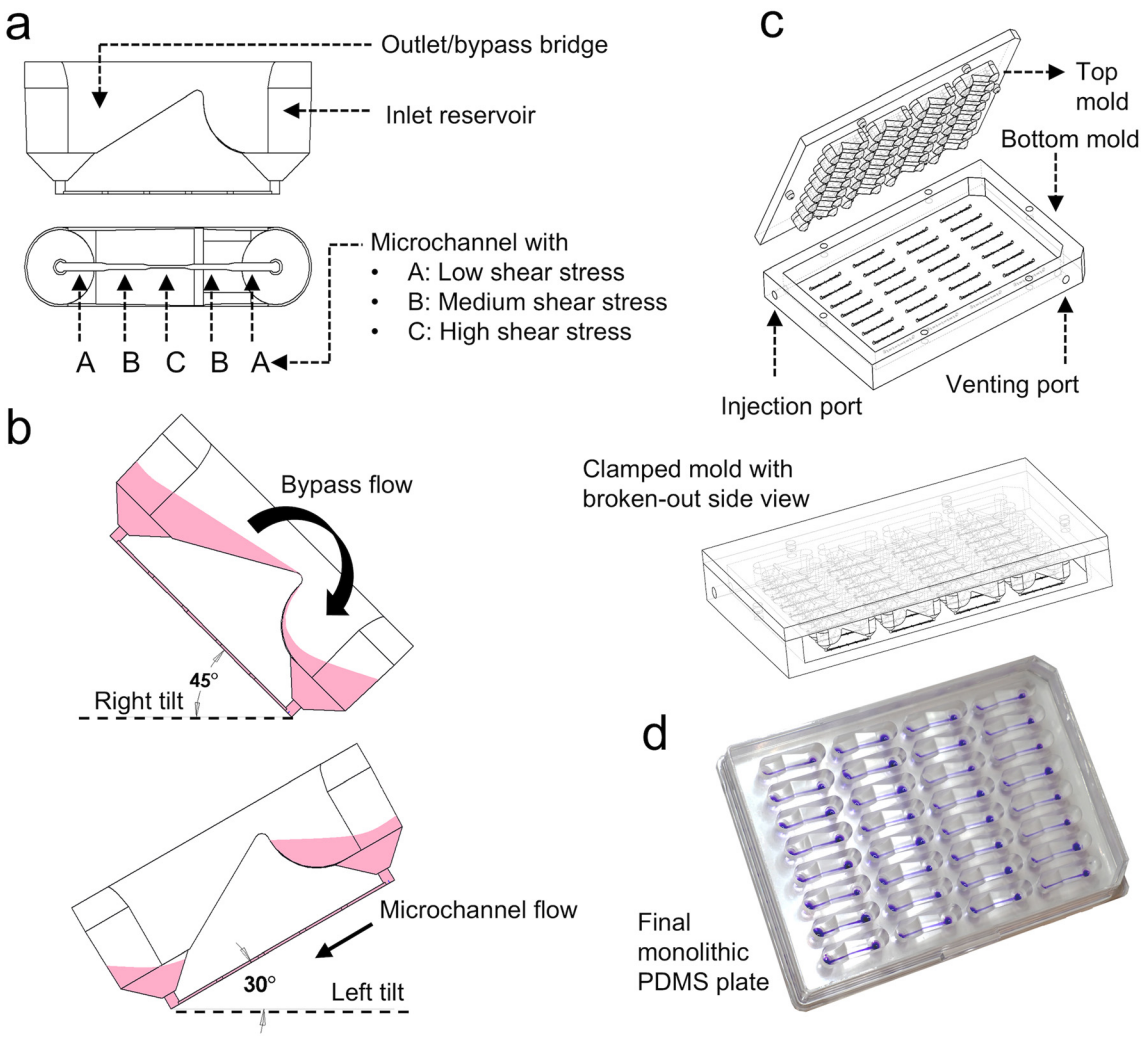

Fig. 1 The microfluidic plate design and fabrication. (a) The sketch of a microfluidic unit of the plate, including the 3D structure of the reservoir (side view) and the microchannel (bottom view). (b) The working principle of the microfluidic design, when the microfluidic unit is tilted to the left at 30°, the liquid (pink) from the inlet reservoir flows through the microchannel, generating shear stress variation at three levels (zones A–C). Following that, after the liquid levels between inlet and outlet reservoirs equilibrate, the microfluidic unit is tilted to the right at 45° so that the liquid is pushed back to the inlet reservoir through the bypass bridge, recirculating the unidirectional flow. (c) Illustration of microfluidic plate fabrication using 3D printing technology and liquid silicone injection molding. (d) The completed PDMS plate having the microchannels filled with violet dye.

the cured mold must be baked at 60 °C for at least 4 h to completely remove all the photoinitiator components within the resin. The photoinitiator inside the resin material is the factor that prohibits the PDMS curing process, resulting in a sticky, non-cured PDMS after molding. Other studies have also reported similar procedures to avoid PDMS curing inhibition.[45] After the post-processing, the mold parts are clamped together and connected to a 60 mL syringe driven by an electric syringe pump set at 9 mL min^{-1}. The syringe is prefilled with PDMS (1 : 10 ratio). After 6 min when the PDMS completely fills the mold and exits through the venting port, the injection is stopped, and the mold is transferred to the oven for baking at 60 °C in 4 h. The cured PDMS slab is then demolded, yielding a 3D structure imprinted within a full monolithic 96-well plate form factor. The cast PDMS plate is plasma bonded (Harrick Plasma) with a 100 μm thin PDMS film (Silex) to seal the microchannel substrate followed by ethanol washing and UV sterilization prior to cell culture. As shown in Fig. 1d, a full microfluidic well plate complying with ANSI/SLAS standard was made.

Table 2 Rocker settings to induce unidirectional and bidirectional flows

Tilt direction	Setting	Unidirectional	Bidirectional
Left	Tilt (°)	30	30
	Speed (RPM)	5	5
	Dwell time (second)	240	240
Right	Tilt (°)	45	30
	Speed (RPM)	10	5
	Dwell time (second)	2	240

Computational and experimental analysis of flow on chip

To perfuse the medium through 32 microchannels simultaneously with precise control of flow rate, using direct air/liquid-tight actuators is unreliable as it requires many tubes, connectors, and

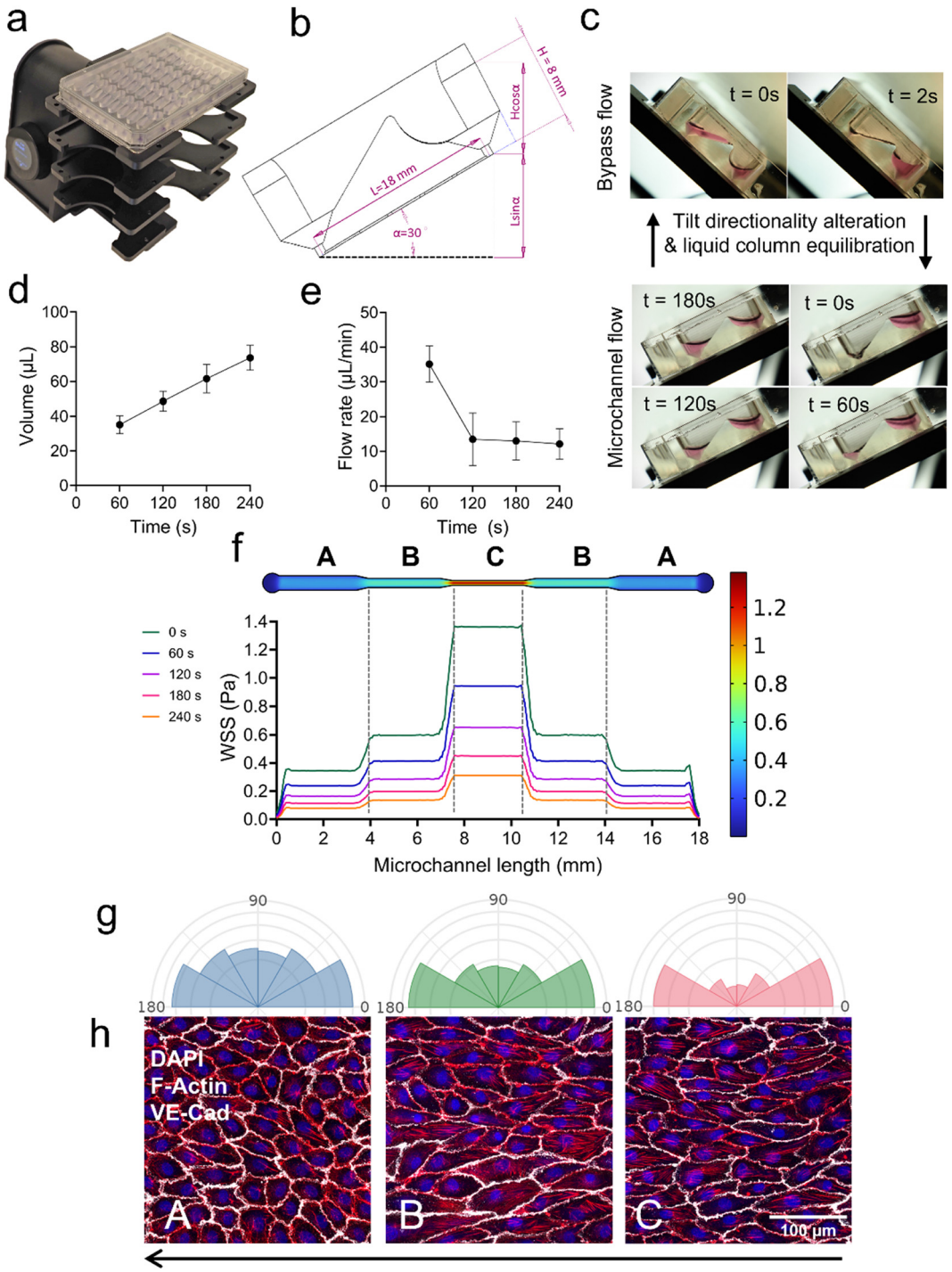

Fig. 2 Characterization of the microfluidic plate performance. (a) The AKITA Wave fully programmable rocker for inducing both uni- and bidirectional flow. The rocker has racks for four plates and can be expanded to a maximum of 16 plates upon need. (b) The sketch showing the working principle of the microfluidic chip. The chip dimensions and tilting angles drive the hydrostatic pressure, regulating flow rate and WSS. (c) The time frames of the fluid perfusion *via* the microchannel and recirculation *via* the reservoirs. The liquid column changes in time and establishes the time-dependent hydrostatic pressure and flow rate. (d) The graph showing the cumulative volume turnover of medium through the microchannel at 30° tilting angle. (e) The graph showing the decay for instantaneous flow rate during one tilting duty cycle. (f) Heat map of the microchannel illustrating the simulation of the symmetrical WSS distribution at the surface of regions of the microchannel: (A, B, and C) line graphs showing the stepwise WSS alteration across the channel length from 0 to 240 s. (g) Half-rose graphs illustrating the cell orientation according to flow direction and WSS magnitudes: A (blue), B (green), and C (red). *n*, two independent experiments. (h) Microscopy images showing the alignments of HUVEC^{GFP} responding to the three WSS levels A, B, and C. The arrow indicates the flow direction. Scale bar: 100 μm. Pseudo-colors in (h): DAPI (blue), F-actin (red), and VE-Cad (white).

multi-channel pumps that make a complicated, non-scalable setup. As an alternative to direct pressure-driven flow, gravity-driven flow was applied as it requires no tubing connections and still allows a uniform flow control across microchannels.[46] As illustrated in Fig. 2a, the plate was mounted on the rack of a fully programmable rocker (AKITA Wave 3.0, Finnadvance). The rocker was set to tilt to the left at 30° so that the inlet reservoir is at a higher level, yielding a hydrostatic pressure difference across the microchannels, initiating the laminar flow.

The sketch of a titled chip illustrating the gravity-driven flow principle is shown in Fig. 2b. At time t = 0 s (Fig. 2c, bottom), the microchannel is filled with cell culture medium, then at 30° tilting, 150 μL of medium is added to the inlet reservoirs while the outlet side is kept empty, inducing an initial height difference between the inlet and outlet liquid column which is

$$\Delta h_0 = H\cos\alpha + L\sin\alpha \tag{2}$$

where H is the inlet reservoir height, L is the microchannel length, and α is the tilt angle. With ρ as the density of the fluid and g as the gravity constant, the initial pressure drop across the microchannel is given as:

$$\Delta P_0 = \rho g(H\cos\alpha + L\sin\alpha) \tag{3}$$

With R as the hydraulic resistance of the channel, we have:

$$Q = \frac{\Delta P}{R} \tag{4}$$

For a pressure difference obtained using liquid columns at different levels, the flow rate can be rewritten as

$$Q = \frac{\rho g \Delta h}{R} \tag{5}$$

One important note is that one must account for the time-dependent effects of the flow in the system, since the hydrostatic pressure-driven flow is not static as the liquid column height decreases in time.[47] The height difference between the inlet and the outlet liquid level Δh is a function of time and is governed by the volumetric flow between the liquid columns.

$$\frac{\mathrm{d}\Delta h}{\mathrm{d}t} = -\frac{2\rho g \Delta h}{AR} \tag{6}$$

Solving this differential equation gives

$$\Delta h(t) = \Delta h_0 e^{-\frac{2\rho g}{AR}t} \tag{7}$$

where A is the cross-sectional area of the liquid column and t is the time. Fig. 2d presents the cumulative volume turnover of liquid passing through the microchannel over time, yielding the changes in liquid column height $\Delta h(t)$ over the period as shown in Fig. 2c. The volume turnover appears linear due to the averaging effect of accumulating volume, even though the instantaneous flow rate varies. In contrast, as $\Delta h(t)$ reduced over time, the instantaneous volumetric flow rate (Fig. 2e) exponentially decays as the hydrostatic pressure difference decreases and the liquid levels between the reservoirs equilibrate. This decline reflects the transient nature of the pressure-driven flow system, where the flow rate diminishes despite the continued accumulation of volume. There we also obtained the time frame in which the liquid from the outlet side was bypassed back to the inlet within 2 s tilting toward the right side (Fig. 2c, top).

To verify the theoretical calculation of flow profiles and map the WSS distribution, COMSOL software was used to numerically simulate the hydrodynamic changes in the microchannels according to the above-mentioned theoretical calculations. A no-slip boundary condition was applied at the walls, laminar inflow with inlet pressure difference according to eqn (3), and zero outlet pressure with suppressed backflow was selected. The volumetric flow rate (the rate at which the volume of fluid passes through a cross-sectional area of the channel) stays the same due to the flow continuity rule; however, the average flow velocity (average distance the fluid particle travels over time) and the WSS along the channel walls increase as the microchannel dimensions become smaller toward the middle region.

Computational WSS distributions across the microchannel regions are illustrated in Fig. 2f. For a tilting angle of α = 30°, the maximum WSS obtained at the three regions A, B, and C are approximately 0.3, 0.6, and 1.3 Pa, respectively. As proof of concept, the HUVEC^{GFP} images at zones A, B, and C are shown in Fig. 2h. After five days of exposure to unidirectional flow, the cells exhibit distinct cell morphology in three zones. The half-rose diagrams in Fig. 2g show that the cells align more with the flow direction as the shear stress increased, as previously published,[48] proving that the established microfluidic design can perform further biological investigation. This range (0.3–1.3 Pa) covers the typical venous shear stress range and dips slightly below it.[49] Thus, our setup is suitable to study for the lower range of the venous pressure to explore how ECs respond to physiological venous flow and non-physiologically slow and bidirectional flow that may occur in VM lesions. The viability of HUVECs and *TIE2*^{WT} iECs were investigated by live-dead staining (Fig. S2†), demonstrating that in both cell types viability was found to be approximately 90% when cultured were under bidirectional flow.

Effects of flow profiles and *TIE2*^{L914F} VM mutation on EC morphology

The hallmark of VMs is low or stagnant blood flow. Due to insufficient perivascular tissue support, changes in posture and pressure from the surrounding tissue may push out blood from lesions after they are refilled slowly. Physiological, unidirectional laminar flow is important for normal vascular morphogenesis;[50] however, the causality of slow flow and aberrant geometry of VM vessels is currently unknown. To test *TIE2*^{L914F} responses to abnormal (static, bidirectional) or normal (unidirectional) flow, the EC morphology (cell area and elongation) of HUVEC^{GFP}, *TIE2*^{WT} HUVEC^{GFP}, and *TIE2*^{L914F} HUVEC^{GFP} were investigated under different WSS and flow profiles (Fig. 3).

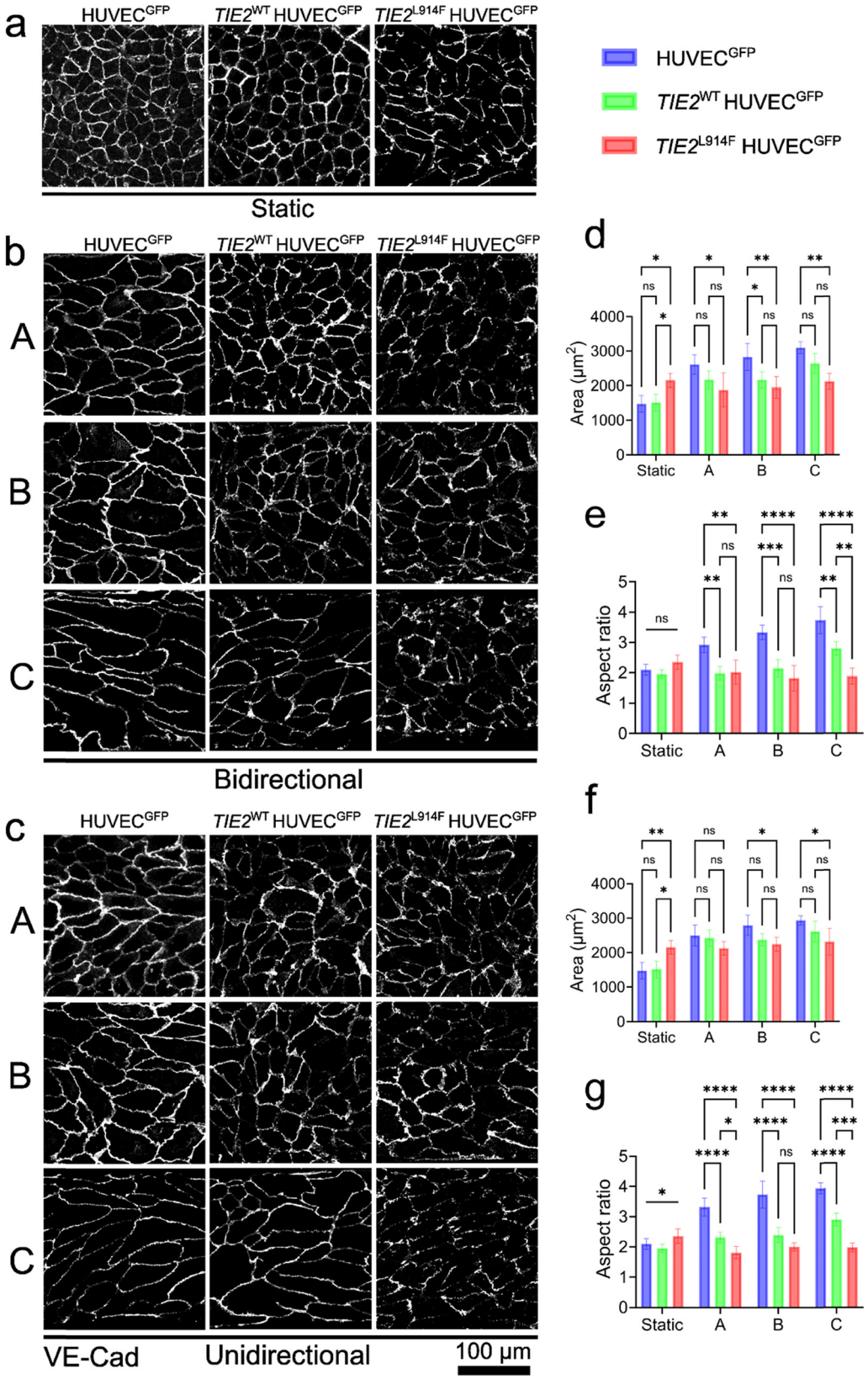

Fig. 3 Analysis of the HUVECs' morphological changes in response to flow variations (zones A–C). The microscopy images of VE-Cad staining from HUVEC^{GFP}, *TIE2*^{WT} HUVEC^{GFP}, and *TIE2*^{L914F} HUVEC^{GFP} under (a) static culture, (b) bidirectional flow, and (c) unidirectional flow, respectively. The graph and statistical analysis of (d) the cell area and (e) the aspect ratio in static and under bidirectional flow. The graph and statistical analysis of (f) the cell area and (g) aspect ratio under static and unidirectional flow. *$P < 0.05$, **$P < 0.01$, ***$P < 0.001$, ****$P < 0.0001$; ns, not statistically significant in two-way ANOVA followed by Tukey's *post hoc* test; *n*, three independent experiments. Vertical coloured line, mean ± SD. Scale bar: 100 μm.

Under static culture, both control HUVECs (HUVEC^{GFP} and *TIE2*^{WT} HUVEC^{GFP}), exhibited a significantly smaller cell area compared to *TIE2*^{L914F} HUVEC^{GFP} as shown in Fig. 3a and d. In bidirectional flow, control HUVECs exhibited a gradual increase in cell area with rising WSS (Fig. 3d). In contrast, *TIE2*^{L914F} HUVECs displayed a consistently lower cell area across all WSS conditions. Under unidirectional flow conditions (Fig. 3c, f and g), a similar trend was observed; HUVEC^{GFP} and *TIE2*^{WT} HUVEC^{GFP} showed a significant increase in cell area with increasing WSS, while *TIE2*^{L914F} HUVEC^{GFP} cell area remained relatively stable regardless of the WSS level. Under static culture, there were no statistically significant differences in cell elongation (the cell aspect ratio) among the three genotypes of HUVECs. Under flow conditions, control HUVEC^{GFP} demonstrated a marked elongation response, with the aspect ratio increasing significantly as WSS escalated (Fig. 3e and g). This elongation confirmed that control HUVEC^{GFP} are highly responsive to WSS in our experimental setting, adapting their morphology accordingly. The consistent trend across both bi-and unidirectional flow conditions indicated that the WSS magnitude, rather than the flow direction, is the determining factor in EC size and elongation. *TIE2*^{WT} HUVEC^{GFP} cells, on the other hand, exhibited a moderate but consistent elongation under all WSS conditions. Their aspect ratio increased with WSS but did not reach the same levels as observed in HUVEC^{GFP}. This indicated a partial responsiveness to WSS, reflecting a functional adaptation that is not as pronounced as in HUVEC^{GFP} that may be due to unavoidable overexpression of *TIE2*^{WT} in the retrovirally transduced HUVEC model. In contrast to these HUVEC controls, *TIE2*^{L914F} HUVEC^{GFP} showed no significant changes in aspect ratio under any flow conditions compared to static culture. This lack of elongation response under WSS, regardless of flow directionality, underscored a defect in these cells to respond to the flow.

It has been shown that fluid shear stress induces phosphorylation of *TIE2*, Akt, Erk1/2 and eNOS in human ECs.[51–54] The same signaling molecules are also chronically activated by the *TIE2*^{L914F} gain-of-function mutation.[29,33,55,56] The lack of responsiveness in *TIE2*^{L914F} HUVECs to WSS can be due to dysfunctional mechanosensory or mechanotransduction signaling pathways due to *TIE2*^{L914F} mutation. Sustainable phosphorylation of signal mediators downstream from mutated *TIE2* may also cause saturation or desensitization of the signaling pathway for sensing the flow. *TIE2*^{WT} activation by its agonistic ligand angiopoietin-1 induces Akt and Erk1/2 activation in specific subcellular compartments.[29,57–60] The *TIE2*^{L914F} is ligand independently active in abnormal subcellular sites[29] likely affecting spatial and temporal activation of Akt, shown to have importance in normal EC response to flow.[61] A previous study by Uebelhoer *et al.* showed that BMP4 was downregulated in *TIE2*^{L914F} in transcriptomic analysis[33] that may also contribute to the dysfunctional response to flow *via* SMAD4 downstream from Akt and BMP4.[62]

Primary ECs, such as HUVECs, are authentic for vascular biology research, they are easy to culture, readily available from commercial vendors and stable genetic modifications are feasible to introduce *via* viral gene transfer. As a technical shortcoming, viral vectors result in unavoidable overexpression of the transferred gene, and heterogeneity and limited passage number of primary ECs restrict their usage. These technical limitations can be overcome by CRISPR/Cas9-based genome editing approaches for the generation of targeted mutation in induced pluripotent stem cell (iPSC)-derived ECs (iECs). Our interest was to investigate iEC responses to bi- and unidirectional flow and the effect of *TIE2*^{L914F} on cell morphology under these conditions. The static cultures (Fig. 4a) indicated no differences between *TIE2*^{WT} and *TIE2*^{L914F} iECs, both in terms of cell area and aspect ratio. Notably, the aspect ratio (*i.e.* elongated cell phenotype) was relatively high when compared to the normal primary ECs (HUVECs), which showed a cuboidal "cobblestone" monolayer morphology in static monolayer culture (Fig. 3a). Under bidirectional flow conditions, *TIE2*^{WT} iECs obtained a more cobblestone shape resembling phenotype (Fig. 4b), suggesting that exposure to the flow promotes iECs to acquire the typical EC shape. *TIE2*^{L914F} iECs exhibited a significantly larger cell area compared to *TIE2*^{WT} iECs across all shear stress levels (0.3 Pa, 0.6 Pa, and 1.3 Pa) in bidirectional mode, similar to our previous study.[21] Under unidirectional flow conditions (Fig. 4c, f and g), a similar trend was observed. *TIE2*^{L914F} iECs consistently showed a significantly larger cell area than *TIE2*^{WT} iECs at all shear stress levels, reinforcing the observation that *TIE2*^{L914F} iECs tend to maintain a larger size regardless of WSS conditions. As a difference to the HUVEC model, *TIE2*^{L914F} iECs responded to bidirectional flow in terms of increased cell area. *TIE2*^{WT} iECs showed a high aspect ratio as a response to both bi- and unidirectional flow, while *TIE2*^{L914F} iECs only in unidirectional flow.

The divergence in responses of HUVECs and iECs under shear stress experiments could have multiple explanations. First, the non-responsiveness in *TIE2*^{L914F} HUVECs and increased sensitivity to flow in *TIE2*^{L914F} iECs may result from the genetic editing process. As discussed above,[61] Akt signaling has a role in normal EC response to flow, which can increase Akt phosphorylation up to 6 times.[51] Due to retroviral transduction, the level of Akt phosphorylation was almost five times higher in *TIE2*^{L914F} HUVECs compared to *TIE2*^{L914F} iECs (Fig. S1†). Therefore, *TIE2*^{L914F} may mask the effect of flow in HUVECs while enhancing the effect of flow in iECs. This assumption is also in line with the published results that in *TIE2*^{L914F} HUVEC^{GFP}, FOXO1 transcription factor downstream of TIE2/Akt pathway was completely cleared from the nucleus while it was only partially cleared in *TIE2*^{L914F} iECs.[21,63] There are also some additional differences between the HUVECs and iECs that may contribute to differential responses. Somatic gain-of-function VM mutations in patients are typically heterozygous. This contrasts with iECs having an endogenously edited *TIE2*^{L914F} on both alleles[21] while HUVECs has intact endogenous TIE2^{WT} alleles additionally overexpressing the *TIE2*^{L914F} or *TIE2*^{WT}. Under static conditions, the aspect ratio in *TIE2*^{WT}

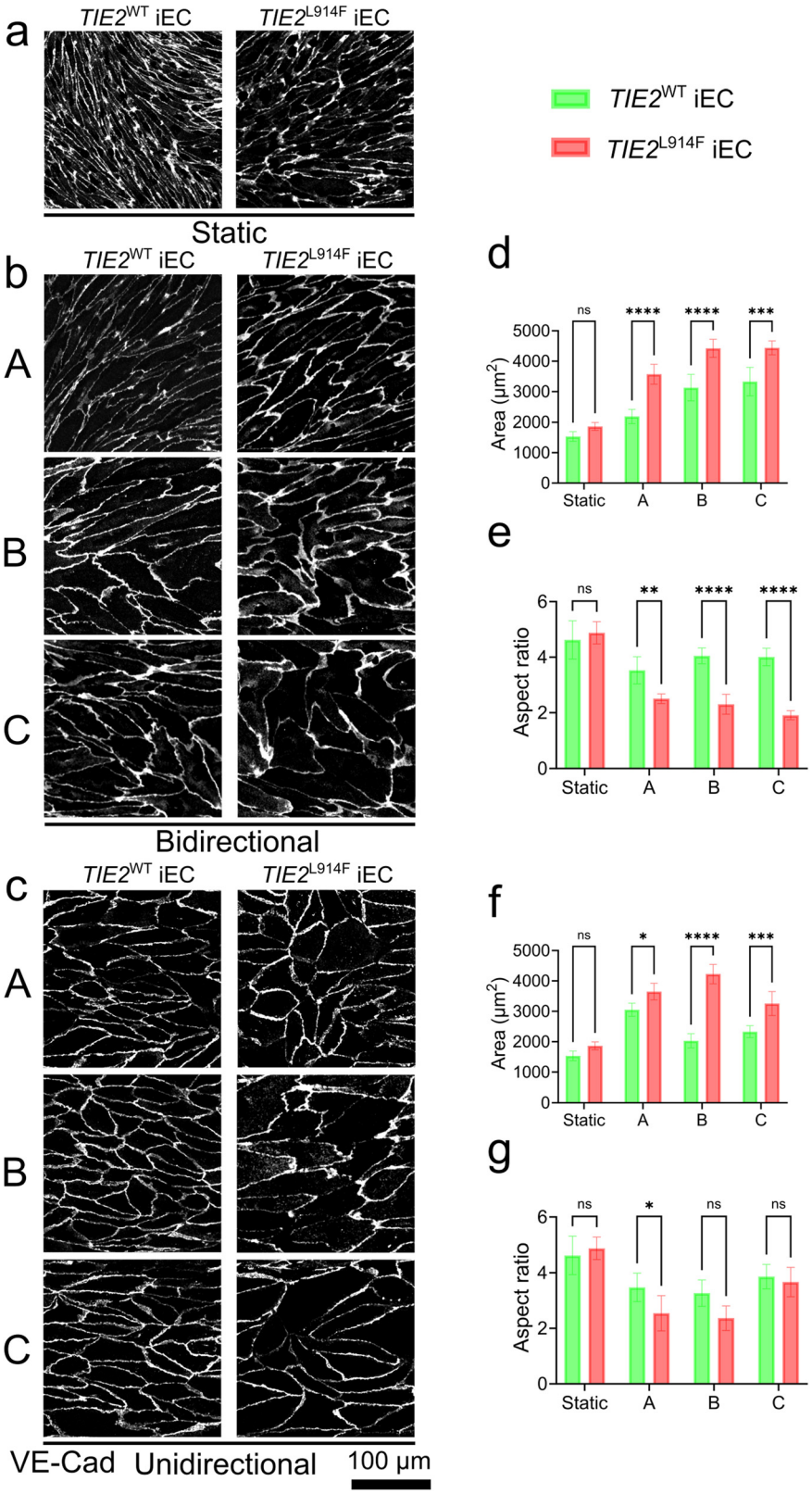

Fig. 4 Analysis of the iECs morphological changes in response to flow variations (zones A–C). Microscopy images of VE-Cad from *TIE2*^{WT} and *TIE2*^{L914F} iECs under (a) static culture, (b) bidirectional and (c) unidirectional condition. The graph and statistical analysis of (d) cell area and (e) aspect ratio under static and bidirectional flow. The graph and statistical analysis of (f) cell area and (g) aspect ratio under static and unidirectional flow. *$P < 0.05$, **$P < 0.01$, ***$P < 0.001$, ****$P < 0.0001$; ns, not statistically significant in two-way ANOVA followed by Tukey's *post hoc* test; *n*, three independent experiments. Vertical coloured line, mean ± SD. Scale bar: 100 μm.

iECs was considerably higher than in HUVEC^{GFP} (both expressing only endogenous *TIE2*), also demonstrating a cell-intrinsic difference between these EC lines. These may include the immaturity of iECs that may not have reached the same level of functional maturity as HUVECs. Furthermore, iECs were not exposed to shear stress during their differentiation, so they may lack the epigenetic memory and morphological adaptations that HUVECs acquire from their *in vivo* exposure to blood flow before isolation from the umbilical cord. Finally, it was also noted that iECs were slightly larger than HUVECs. This larger surface area exposed to mechanical influence from flow may contribute to the quicker cellular alignment observed in iECs.

Flow profiles induce differentiated directionality of F-actin

The F-actin analysis under static and dynamic conditions (bi- and unidirectional) demonstrated that actin filaments respond to both direction and magnitude of shear stress applied to HUVECs and iECs. Under static conditions, the F-actin filaments in the control HUVECs (HUVEC^{GFP}, *TIE2*^{WT} HUVEC^{GFP}) and in *TIE2*^{L914F} HUVEC^{GFP} had similar length and were arranged in a non-aligned manner as they did not show orientation in any specific direction (Fig. 5a, d and g). Also, phalloidin staining showed a prominent cortical actin rim in control HUVECs that was almost absent in *TIE2*^{L914F} (Fig. 5a). With the induction of flow, the F-actin filaments in HUVEC^{GFP} began to align with the flow direction both in bi- and unidirectional schemes starting at the lowest WSS level of 0.3 Pa, and this alignment increased progressively with higher WSS levels. Meanwhile, *TIE2*^{WT} HUVEC^{GFP} exhibited a moderate increase in F-actin alignment in both flow conditions. Even though there is a similar trend in F-actin alignment of HUVEC^{GFP} and *TIE2*^{WT} HUVEC^{GFP} under both bi- and unidirectional flow, the unidirectional flow enforces the cells to align more, highlighting the importance of directionality of the flow. This finding emphasizes that both the magnitude and the directionality of flow affect the cell's cytoskeleton arrangements. In contrast to the control HUVECs, *TIE2*^{L914F} HUVEC^{GFP} showed no change due to flow induction. In zone B, where the WSS was 0.6 Pa, the length of actin filaments remained similar to that in zone A, showing no significant F-actin elongation (Fig. 5j). Additionally, the actin filaments in *TIE2*^{L914F} HUVEC^{GFP} were significantly shorter than those in control HUVECs under bidirectional flow. In zone C, where the shear stress was highest at 1.3 Pa, in control HUVECs, F-actin become longer than those in *TIE2*^{L914F} HUVEC^{GFP}. In contrast, the actin filaments in *TIE2*^{L914F} HUVEC^{GFP} were not influenced by the flow, even at the highest shear stress, neither in terms of size nor orientation. Furthermore, in *TIE2*^{L914F} HUVEC^{GFP}, F-actin filaments were fragmented, with low average length regardless of flow conditions.

Notably, VE-Cad was also disorganized in *TIE2*^{L914F} HUVEC^{GFP} (Fig. 3b and c) which may contribute to the failure of actin filament orientation with flow. It has been shown that HUVECs are able to sense flow direction, *e.g.* through β1 integrin, exhibiting distinct responses to bi- and unidirectional flow (1.5 Pa) in the dish connected to the syringe pump system. Also, in the same study, both *in vitro* and *in vivo*, ECs showed greater alignment with unidirectional flow compared to bidirectional flow,[64] consistent with our observations (Fig. 5).

In iECs, under bidirectional mode, both *TIE2*^{WT} iECs and *TIE2*^{L914F} iECs showed a trend of longer actin filaments compared to the static, however, the difference was more significant for *TIE2*^{L914F} iECs. Upon flow induction in zone A, the *TIE2*^{L914F} iECs exhibited significant actin filament elongation, while the *TIE2*^{WT} iECs did not show significant elongation compared to static conditions (Fig. 6a and b). The *TIE2*^{WT} iECs displayed significantly longer actin filaments only in zones B and C, indicating that WSS in zone A was insufficient for elongation. Additionally, both iEC genotypes showed a trend of orienting with flow direction under bidirectional conditions. *TIE2*^{L914F} iECs showed a higher level of F-actin alignment than *TIE2*^{WT} iECs in all zones (Fig. 6b and g). F-actin filaments of *TIE2*^{WT} iECs oriented with the flow only in zone C, where the WSS is highest (Fig. 6e and g), although it was still significantly lower than *TIE2*^{L914F} iECs.

The effect of flow on F-actin in iECs was more distinct under unidirectional mode. In unidirectional mode, both iEC genotypes showed a better F-actin alignment in response to WSS. In zone A, *TIE2*^{WT} iECs oriented with flow, while *TIE2*^{L914F} iECs failed to do so (Fig. 6c and i). However, in zones B and C, where the shear stress was higher, both *TIE2*^{L914F} iECs and *TIE2*^{WT} iECs oriented with the flow, with no significant difference between them in terms of actin orientation. This non-responsiveness of *TIE2*^{L914F} iECs observed in zone A started to decrease, and *TIE2*^{L914F} iECs became responsive with higher shear stress in zone B and zone C.

The actin filament arrangement of *TIE2*^{L914F} iECs was distinct from that of *TIE2*^{L914F} HUVEC^{GFP}, as *TIE2*^{L914F} iECs oriented with the flow in medium and high shear stress under unidirectional flow, while *TIE2*^{L914F} HUVEC^{GFP} did not react to flow. As discussed above, the difference may be due to EC cell type-intrinsic differences[3,65] and/or because of higher magnitude of the gain-of-function effect of *TIE2*^{L914F} mutation in HUVECs.

Effect of *TIE2*^{L914F} mutation and flow on endothelial cell polarity

To analyze the cell polarity in control and *TIE2*^{L914F} expressing ECs in different flow conditions we next analyzed the Golgi nucleus orientation that has been used as a read-out for EC responsiveness to WSS.[66] The Golgi localization relative to the nucleus was investigated microscopically and the cells were categorized based on Golgi localization as shown in Fig. 7a–c. Under static culture, the Golgi apparatus in all genotypes in both HUVECs and iECs were polarizing randomly as illustrated by the rose diagrams in Fig. 7d. None of the cell lines showed Golgi polarization in bidirectional flow condition similar to static mode.

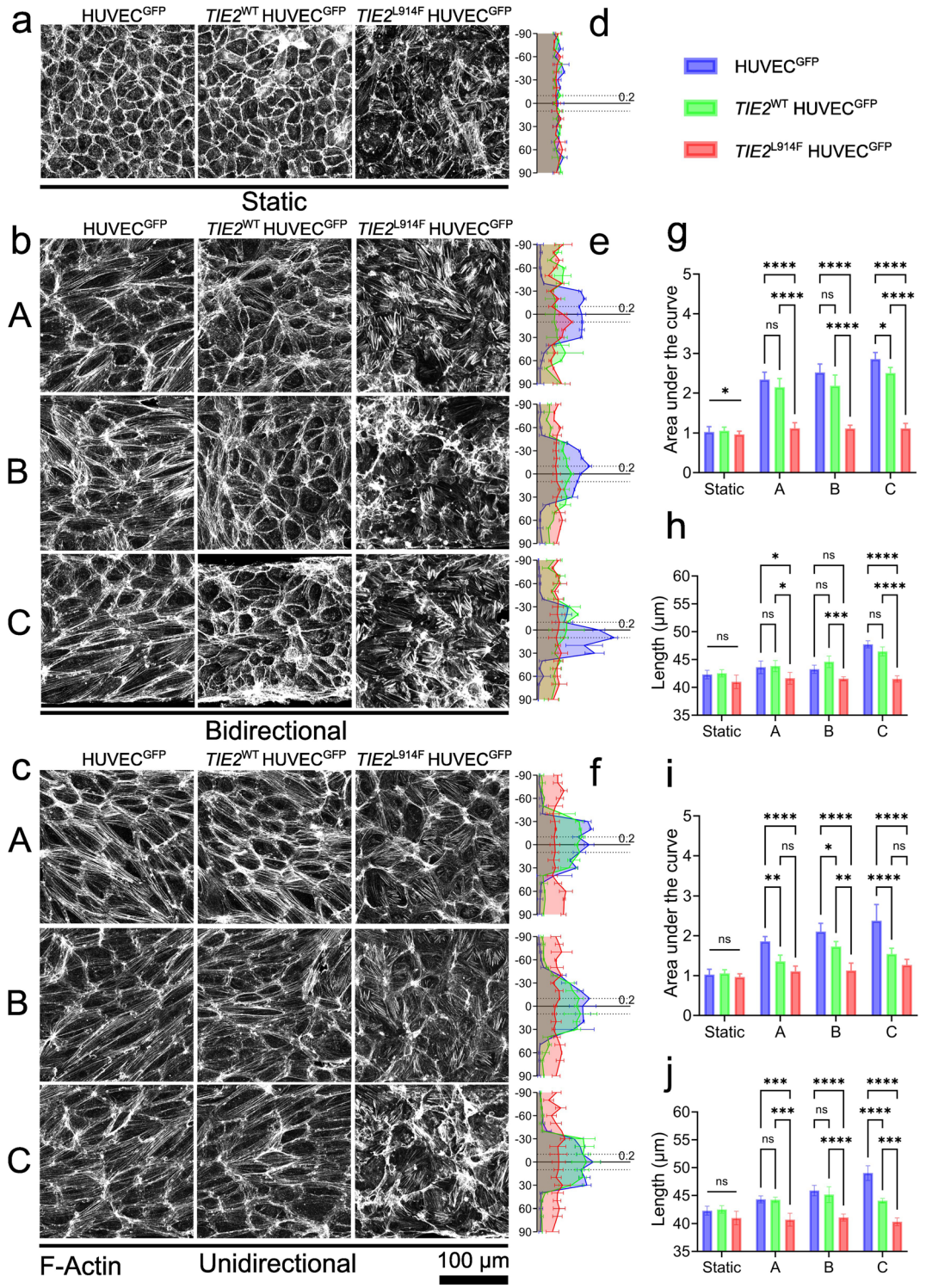

Fig. 5 Analysis of the HUVECs' F-actin rearrangement in response to flow variations. F-actin microscopy images of the HUVEC^{GFP}, *TIE2*^{WT} and *TIE2*^{L914F} under (a) static, (b) bidirectional and (c) unidirectional flow. The distribution of F-actin orientation under (d) static, (e) bidirectional, and (f) unidirectional culture mode. The graphs show the area under the curve and statistical analysis in F-actin orientation distribution within ±10° in response to (g) bidirectional and (i) unidirectional flow. The graphs and statistical analysis of the F-actin length under (h) bidirectional and (j) unidirectional flow. *$P < 0.05$, **$P < 0.01$, ***$P < 0.001$, ****$P < 0.0001$; ns, not statistically significant in two-way ANOVA followed by Tukey's *post hoc* test; *n*, three independent experiments. Vertical coloured line, mean ± SD. Scale bar: 100 μm.

With the induction of unidirectional flow, control HUVECs (HUVEC^{GFP} and *TIE2*^{WT} HUVEC^{GFP}) predominantly exhibited upstream Golgi polarization, aligning the Golgi apparatus against the direction of the flow, which is a typical

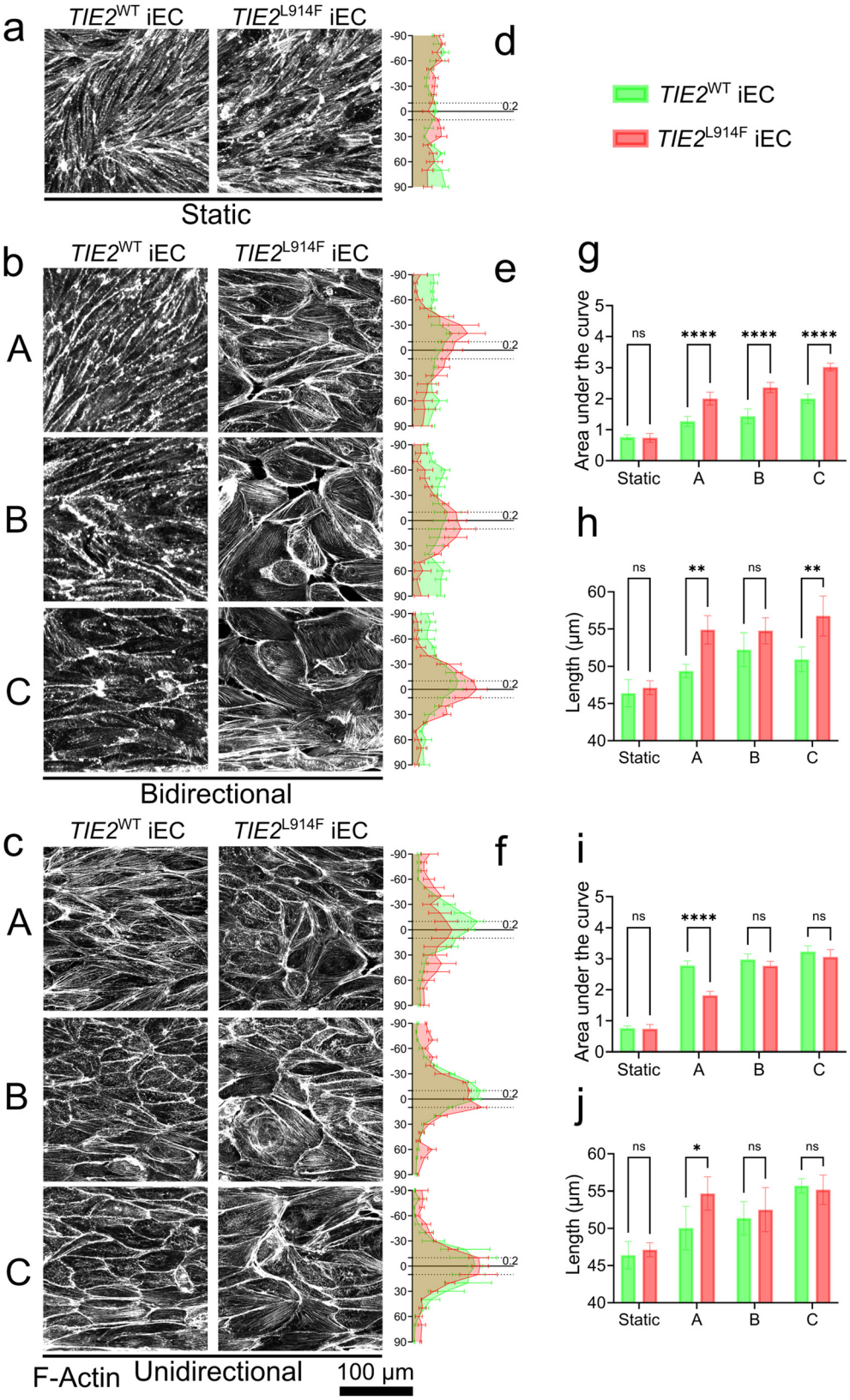

Fig. 6 Analysis of the *TIE2*^{WT} and *TIE2*^{L914F} iECs' F-actin rearrangement in response to flow variations. Microscopy images of F-actin from *TIE2*^{WT} and *TIE2*^{L914F} iECs under (a) static culture and (b) bidirectional and (c) unidirectional flow. Distribution of F-actin orientation under (d) static culture and (e) bidirectional and (f) unidirectional flow. The graphs show the area under the curve and statistical analysis in F-actin orientation distribution within ±10° in response to (g) bidirectional and (i) unidirectional flow. The graphs and statistical analysis of the F-actin length under (h) bidirectional and (j) unidirectional flow. *$P < 0.05$, **$P < 0.01$, ***$P < 0.001$, ****$P < 0.0001$; ns, not statistically significant in two-way ANOVA followed by Tukey's *post hoc* test; *n*, three independent experiments. Vertical coloured line, mean ± SD. Scale bar: 100 µm.

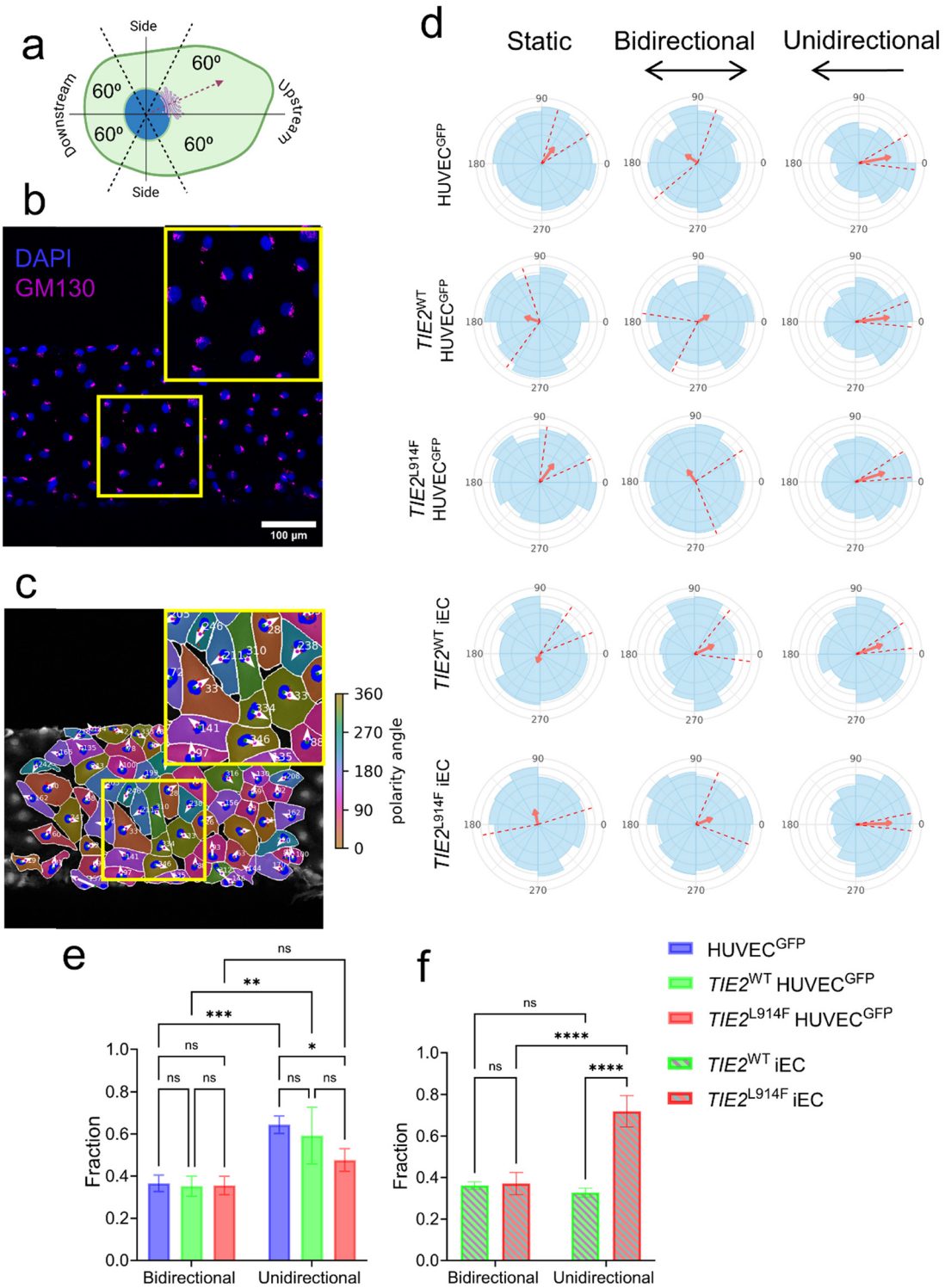

Fig. 7 Analysis of the HUVECs' and iECs' Golgi apparatus polarization in response to flow variations. (a) Explanation of the Golgi polarization orientation, the vector connecting the centers of mass of the nucleus to Golgi with the horizontal axis forming the polarization angle. Assuming the angle of flow direction is 180° from right to left, the Golgi can be located within 4 depicted zones: upstream, downstream, and two sides. (b) Representative image of DAPI (blue) merged with Golgi (GM130, magenta) of HUVECs, showing the polarization of the Golgi with respect to the nuclei. (c) The plot of the segmented image including the orientation vector from the nuclei to the Golgi apparatus. The mask with orientation vectors was generated by PolarityJaM tool. (d) Distribution of Golgi polarity of the HUVECs and iECs under static, bi- and unidirectional flows. Rose graphs generated by the PolarityJaM Web app from zone C of the microfluidic channels; red arrows indicate the mean direction of Golgi polarization. The red dashed lines indicate 95% confidence intervals. The quantification of upstream proportion of different genotypes of (e) HUVECs and (f) iECs under the bi- and unidirectional flow conditions. The graph combines data from 3 zones A, B and C of each channel. $*P < 0.05$, $**P < 0.01$, $***P < 0.001$, $****P < 0.0001$; ns, not statistically significant in two-way ANOVA followed by Tukey's *post hoc* test; *n*, three independent experiments. Vertical coloured line, mean ± SD. Scale bar: 100 μm.

endothelial response to shear stress.[14,67] In *TIE2*^{L914F}, the fraction of polarized cells was less than in HUVEC^{GFP}. The comparison between bi- and unidirectional Golgi polarization responses indicated that the Golgi polarization required to be exposed to flow only in one direction without periodic change in flow direction. In contrast to the HUVEC model, *TIE2*^{WT} iECs did not exhibit stronger upstream polarization in unidirectional flow, while the response was significantly stronger in *TIE2*^{L914F} iECs (Fig. 7d–f). The retroviral *TIE2*^{L914F} mutation hindered Golgi polarization in HUVECs, while locus-targeted *TIE2*^{L914F} accelerated Golgi polarization under unidirectional flow. This disparity in responses to the same mutation may be attributed to the differences in gene expression levels resulting from the retroviral overexpression *versus* locus-specific targeting, considering the critical role of *TIE2* and its signaling pathways in mechanosensing.[51,54,68] Additionally, the arterial characteristics of *TIE2*^{L914F} iECs and the venous origin of *TIE2*^{L914F} HUVEC^{GFP} may contribute to their distinct responses.[21] Furthermore, variations in the composition and thickness of podocalyxin, a known mechanosensor, have been identified as contributing to different mechanosensing responses in HUVECs and iECs.[65] All in all, both *TIE2*^{L914F} HUVEC^{GFP} and *TIE2*^{L914F} iECs have their advantages and limitations. In the former, retroviral transduction results in high transfection efficacy and stable expression of transferred gene but also unavoidable overexpression that may affect results. In iECs, lifespan is less limited and genome editing is more feasible than in primary ECs; however, iECs can be influenced by incomplete epigenetic reprogramming and exhibits a spindle cell-like phenotype rather than the EC typical cobblestone appearance.[21] Future research using patient or gene targeted mouse-derived VM ECs could offer deeper insights into whether HUVEC *TIE2*^{L914F} or iEC *TIE2*^{L914F} model better mimicked authentic VM ECs.

Conclusions

This study presents a novel microfluidic chip design capable of inducing pumpless unidirectional flow in a standardized well plate format, offering scalability to higher throughput capabilities. The investigation delves into the responses of two different types of ECs under static, bi-, and unidirectional flow conditions and investigation of *TIE2*^{L914F} gain-of-function mutation for better understanding of the EC dysfunctions in VMs, where blood flow is notably slow.

Comparison of control and *TIE2*^{L914F} expressing ECs underscored the importance of controlled *TIE2* signaling in the sensing of flow directionality and WSS magnitude. We also observed significant differences between HUVEC and iEC models, which could be attributed to the type of genetic engineering, expression level of the *TIE2*^{L914F} mutation, the endothelial maturity, and inherent variations in mechanosensory pathways or adaptations of the cells to their environment by epigenetic memory. The distinctive response to flow underscores the need for further investigations to elucidate the divergent mechanosensory mechanisms between iECs and HUVECs.

As a summary, the developed platform allowed the characterization of EC phenotypes including cell polarity, proliferation, cytoskeleton arrangement and responses to flow in a microenvironment mimicking normal and diseased vessels and provided quantifiable phenotypic and molecular read-outs for a vascular disease.

Data availability

Data for this article, including the flow rate, volume measurements, wall shear stress (WSS) values presented in Fig. 2d–f are available at **https://zenodo.org/doi/10.5281/zenodo.13383280**. The other data supporting this article have been included as part of the ESI.†

Author contributions

Conceptualization: M. A., H.-T. N., P. S., L. E. Funding acquisition: R. H., P. S., L. E. Methodology: M. A., H.-T. N., B. L., P. S., L. E. Resources: P. S., R. H., L. E. Software: J. K., H.-T. N. Investigation: B. L., J. K., L. S., R. S., P. J., S.-L. R., M. A., H.-T. N. Visualization: M. A., H.-T. N. Supervision: R. H., P. S., L. E. Writing – original draft: M. A., B. L., H.-T. N. Writing – review & editing: M. A., B. L., H.-T. N., P. S., R. H., L. E.

Conflicts of interest

H.-T. N., J. K., P. J., and P. S. are all Finnadvance employees and hold stock options. B. L and R. H. are AstraZeneca employees. R. H. is an AstraZeneca shareholder.

Acknowledgements

The research leading to these results received funding from the European Union's Horizon 2020 research and innovation program under the Marie Skłodowska-Curie grant agreement 814316 (M. A., H.-T. N., B. L., R. H., P. S., and L. E.), the Finnish Cultural Foundation (M. A.), and the Research Council of Finland Flagship program 359344 (M. A. and L. E.).

References

1 D. A. Chistiakov, A. N. Orekhov and Y. V. Bobryshev, Effects of shear stress on endothelial cells: go with the flow, *Acta Physiol.*, 2017, **219**(2), 382–408, DOI: **10.1111/apha.12725**.
2 R. Steward, D. Tambe, C. Corey Hardin, R. Krishnan and J. J. Fredberg, Fluid shear, intercellular stress, and endothelial cell alignment, *Am. J. Physiol.*, 2015, **308**(8), C657–C664, DOI: **10.1152/ajpcell.00363.2014**.
3 S. Arora, A. J. Y. Lam, C. Cheung, E. K. F. Yim and Y. C. Toh, Determination of critical shear stress for maturation of human pluripotent stem cell-derived endothelial cells towards an arterial subtype, *Biotechnol. Bioeng.*, 2019, **116**(5), 1164–1175, DOI: **10.1002/bit.26910**.
4 S. Kim, M. Chung, J. Ahn, S. Lee and N. L. Jeon, Interstitial flow regulates the angiogenic response and phenotype of

endothelial cells in a 3D culture model, *Lab Chip*, 2016, **16**, 4189–4199, DOI: **10.1039/c6lc00910g**.

5 C. Zaragoza, S. Márquez and M. Saura, Endothelial mechanosensors of shear stress as regulators of atherogenesis, *Curr. Opin. Lipidol.*, 2012, **23**(5), 446–452, DOI: **10.1097/MOL.0b013e328357e837**.

6 R. Białecki, W. Adamczyk, D. Borys, J. Głowacki, M. Gracka, B. Melka, K. Psiuk-Maksymowicz, Z. Ostrowski, M. Rojczyk and J. Wasilewski, Blood flow in deforming vessels, *J. Phys.: Conf. Ser.*, 2024, **2766**, 012191, DOI: **10.1088/1742-6596/2766/1/012191**.

7 C. A. Dessalles, C. Ramón-Lozano, A. Babataheri and A. I. Barakat, Luminal flow actuation generates coupled shear and strain in a microvessel-on-chip, *Biofabrication*, 2022, **14**, 015003, DOI: **10.1088/1758-5090/ac2baa**.

8 T. Q. Nguyen and W.-T. Park, Fabrication method of multi-depth circular microchannels for investigating arterial thrombosis-on-a-chip, *Sens. Actuators, B*, 2020, **321**, 128590, DOI: **10.1016/j.snb.2020.128590**.

9 H. Yang, T. Chen, Y. Hu, F. Niu, X. Zheng, H. Sun, L. Cheng and L. Sun, A microfluidic platform integrating dynamic cell culture and dielectrophoretic manipulation for in situ assessment of endothelial cell mechanics, *Lab Chip*, 2023, **23**, 3581–3592, DOI: **10.1039/D3LC00363A**.

10 F. Chesnais, J. Joel, J. Hue, S. Shakib, L. Di Silvio, A. E. Grigoriadis, T. Coward and L. Veschini, Continuously perfusable, customisable, and matrix-free vasculature on a chip platform, *Lab Chip*, 2023, **23**, 761–772, DOI: **10.1039/D2LC00930G**.

11 H. Heidari, H. Taylor and Y. Daghighi, Micro-engineering a platform to reconstruct physiology and functionality of the human brain microvasculature in vitro, *Microfluidics, BioMEMS, and Medical Microsystems XVI*, 2018, p. 23, DOI: **10.1117/12.2291838**.

12 A. Ramirez, M. Amosu, P. Lee and K. Maisel, Microfluidic systems to study tissue barriers to immunotherapy, *Drug Delivery Transl. Res.*, 2021, **11**, 2414–2429, DOI: **10.1007/s13346-021-01016-2**.

13 Z. Wan, A. X. Zhong, S. Zhang, G. Pavlou, M. F. Coughlin, S. E. Shelton, H. T. Nguyen, J. H. Lorch, D. A. Barbie and R. D. Kamm, A Robust Method for Perfusable Microvascular Network Formation In Vitro, *Small Methods*, 2022, **6**, 2200143, DOI: **10.1002/smtd.202200143**.

14 U. M. Sonmez, Y.-W. Cheng, S. C. Watkins, B. L. Roman and L. A. Davidson, Endothelial cell polarization and orientation to flow in a novel microfluidic multimodal shear stress generator, *Lab Chip*, 2020, **20**, 4373–4390, DOI: **10.1039/D0LC00738B**.

15 A. Sivarapatna, M. Ghaedi, Y. Xiao, E. Han, B. Aryal, J. Zhou, C. Fernandez-Hernando, Y. Qyang, K. K. Hirschi and L. E. Niklason, Engineered Microvasculature in PDMS Networks Using Endothelial Cells Derived from Human Induced Pluripotent Stem Cells, *Cell Transplant.*, 2017, **26**, 1365–1379, DOI: **10.1177/096368971772028**.

16 H. L. Ma, A. C. Urbaczek, F. Zeferino Ribeiro De Souza, P. Augusto Gomes Garrido Carneiro Leão, J. Rodrigues Perussi and E. Carrilho, Rapid Fabrication of Microfluidic Devices for Biological Mimicking: A Survey of Materials and Biocompatibility, *Micromachines*, 2021, **12**, 346, DOI: **10.3390/mi12030346**.

17 A. Vivas, J. Mikhal, G. M. Ong, A. Eigenbrodt, A. D. Van Der Meer, R. Aquarius, B. J. Geurts and H. D. Boogaarts, Aneurysm-on-a-Chip: Setting Flow Parameters for Microfluidic Endothelial Cultures Based on Computational Fluid Dynamics Modeling of Intracranial Aneurysms, *Brain Sci.*, 2022, **12**, 603, DOI: **10.3390/brainsci12050603**.

18 K. Hattori, Y. Munehira, H. Kobayashi, T. Satoh, S. Sugiura and T. Kanamori, Microfluidic perfusion culture chip providing different strengths of shear stress for analysis of vascular endothelial function, *J. Biosci. Bioeng.*, 2014, **118**, 327–332, DOI: **10.1016/j.jbiosc.2014.02.006**.

19 V. Van Duinen, A. Van Den Heuvel, S. J. Trietsch, H. L. Lanz, J. M. Van Gils, A. J. Van Zonneveld, P. Vulto and T. Hankemeier, 96 perfusable blood vessels to study vascular permeability in vitro, *Sci. Rep.*, 2017, **7**, 18071, DOI: **10.1038/s41598-017-14716-y**.

20 W. J. Polacheck, M. L. Kutys, J. B. Tefft and C. S. Chen, Microfabricated blood vessels for modeling the vascular transport barrier, *Nat. Protoc.*, 2019, **14**, 1425–1454, DOI: **10.1038/s41596-019-0144-8**.

21 B. Lazovic, H.-T. Nguyen, M. Ansarizadeh, L. Wigge, F. Kohl, S. Li, M. Carracedo, J. Kettunen, L. Krimpenfort, R. Elgendy, K. Richter, L. De Silva, B. Bilican, P. Singh, P. Saxena, X. Hong, L. Eklund and R. Hicks, Human iPSC and CRISPR targeted gene knock-in strategy for studying the somatic $TIE2^{L914F}$ mutation in endothelial cells, *Angiogenesis*, 2024, **27**, 523–542, DOI: **10.1007/s10456-024-09925-9**.

22 C. Remmert, M. Otgonbayar, J. A. Perschel, M. Marder and M. Meier, Protocol to generate a microfluidic vessels-on-chip platform using human pluripotent stem cell-derived endothelial cells, *STAR Protoc.*, 2024, **5**, 103300, DOI: **10.1016/j.xpro.2024.103300**.

23 Y. I. Wang and M. L. Shuler, UniChip enables long-term recirculating unidirectional perfusion with gravity-driven flow for microphysiological systems, *Lab Chip*, 2018, **18**, 2563–2574, DOI: **10.1039/C8LC00394G**.

24 F. Zhang, D. S. Y. Lin, S. Rajasekar, A. Sotra and B. Zhang, Pump-Less Platform Enables Long-Term Recirculating Perfusion of 3D Printed Tubular Tissues, *Adv. Healthcare Mater.*, 2023, **12**, 2300423, DOI: **10.1002/adhm.202300423**.

25 G. S. Offeddu, J. C. Serrano, S. W. Chen, S. E. Shelton, Y. Shin, M. Floryan and R. D. Kamm, Microheart: A microfluidic pump for functional vascular culture in microphysiological systems, *J. Biomech.*, 2021, **119**, 110330, DOI: **10.1016/j.jbiomech.2021.110330**.

26 M. J. Schonning, S. Koh, R. W. Sun, G. T. Richter, A. K. Edwards, C. J. Shawber and J. K. Wu, Venous malformation vessels are improperly specified and hyperproliferative, *PLoS One*, 2021, **16**, e0252342, DOI: **10.1371/journal.pone.0252342**.

27 M. Vikkula, L. M. Boon, K. L. C. Iii, J. T. Calvert, A. J. Diamonti, B. Goumnerov, K. A. Pasyk, D. A. Marchuk, M. L. Warman, L. C. Cantley, J. B. Mulliken and B. R. Olsen,

Vascular dysmorphogenesis caused by an activating mutation in the receptor tyrosine kinase TIE2, *Cell*, 1996, **87**(7), 1181–1190, DOI: **10.1016/s0092-8674(00)81814-0**.

28 Z. Du, J. Zheng, Z. Zhang and Y. Wang, Review of the endothelial pathogenic mechanism of TIE2-related venous malformation, *J. Vasc. Surg. Venous Lymphat. Disord.*, 2017, **5**, 740–748, DOI: **10.1016/j.jvsv.2017.05.001**.

29 M. Nätynki, J. Kangas, I. Miinalainen, R. Sormunen, R. Pietilä, J. Soblet, L. M. Boon, M. Vikkula, N. Limaye and L. Eklund, Common and specific effects of TIE2 mutations causing venous malformations, *Hum. Mol. Genet.*, 2015, **24**(22), 6374–6389, DOI: **10.1093/hmg/ddv349**.

30 E. Seront, M. Vikkula and L. M. Boon, Venous Malformations of the Head and Neck, *Otolaryngol. Clin. N. Am.*, 2018, **51**, 173–184, DOI: **10.1016/j.otc.2017.09.003**.

31 N. Limaye, V. Wouters, M. Uebelhoer, M. Tuominen, R. Wirkkala, J. B. Mulliken, L. Eklund, L. M. Boon and M. Vikkula, Somatic mutations in angiopoietin receptor gene TEK cause solitary and multiple sporadic venous malformations, *Nat. Genet.*, 2009, **41**, 118–124, DOI: **10.1038/ng.272**.

32 Y. Cai, S. Schrenk, J. Goines, G. E. Davis and E. Boscolo, Constitutive Active Mutant TIE2 Induces Enlarged Vascular Lumen Formation with Loss of Apico-basal Polarity and Pericyte Recruitment, *Sci. Rep.*, 2019, **9**, 12352, DOI: **10.1038/s41598-019-48854-2**.

33 M. Uebelhoer, M. Nätynki, J. Kangas, A. Mendola, H.-L. Nguyen, J. Soblet, C. Godfraind, L. M. Boon, L. Eklund, N. Limaye and M. Vikkula, Venous malformation-causative TIE2 mutations mediate an AKT-dependent decrease in PDGFB, *Hum. Mol. Genet.*, 2013, **22**, 3438–3448, DOI: **10.1093/hmg/ddt198**.

34 M. Mishra, G. Singh, A. Gaur, S. Tandon and A. Singh, Role of sclerotherapy in management of vascular malformation in the maxillofacial region: Our experience, *Natl. J. Maxillofac. Surg.*, 2017, **8**, 64, DOI: **10.4103/0975-5950.208973**.

35 J. L. Orlando, J. G. M. P. Caldas, H. G. D. A. Campos, K. Nishinari, M. Krutman and N. Wolosker, Ethanol sclerotherapy of head and neck venous malformations, *Einstein*, 2014, **12**, 181–186, DOI: **10.1590/S1679-45082014AO2844**.

36 J. Y. Ryu, P. S. Eo, J. S. Lee, J. W. Lee, S. J. Lee, J. M. Lee, S. Y. Lee, S. Huh, J. Y. Kim and H. Y. Chung, Surgical approach for venous malformation in the head and neck, *Arch. Craniofac. Surg.*, 2019, **20**, 304–309, DOI: **10.7181/acfs.2019.00416**.

37 C. Poon, Measuring the density and viscosity of culture media for optimized computational fluid dynamics analysis of in vitro devices, *J. Mech. Behav. Biomed. Mater.*, 2022, **126**, 105024, DOI: **10.1016/j.jmbbm.2021.105024**.

38 J. Schindelin, I. Arganda-Carreras, E. Frise, V. Kaynig, M. Longair, T. Pietzsch, S. Preibisch, C. Rueden, S. Saalfeld, B. Schmid, J.-Y. Tinevez, D. J. White, V. Hartenstein, K. Eliceiri, P. Tomancak and A. Cardona, Fiji: an open-source platform for biological-image analysis, *Nat. Methods*, 2012, **9**, 676–682, DOI: **10.1038/nmeth.2019**.

39 C. Stringer, T. Wang, M. Michaelos and M. Pachitariu, Cellpose: a generalist algorithm for cellular segmentation, *Nat. Methods*, 2021, **18**, 100–106, DOI: **10.1038/s41592-020-01018-x**.

40 L. Hauke, A. Primeßnig, B. Eltzner, J. Radwitz, S. F. Huckemann and F. Rehfeldt, FilamentSensor 2.0: An open-source modular toolbox for 2D/3D cytoskeletal filament tracking, *PLoS One*, 2023, **18**, e0279336, DOI: **10.1371/journal.pone.0279336**.

41 W. Giese, J. P. Albrecht, O. Oppenheim, E. B. Akmeriç, J. Kraxner, D. Schmidt, K. Harrington and H. Gerhardt, PolarityJaM: An image analysis toolbox for cell polarity, junction and morphology quantification, *bioRxiv*, 2024, preprint, 01.24.577027, DOI: **10.1101/2024.01.24.577027**.

42 M. M. N. Hossain, N.-W. Hu, W. Murfee and P. Balogh, Three-Dimensional Shear Stress Characteristics in Angiogenic Microvascular Networks Revealed Through Red Blood Cell-Resolved Modeling Based on Real Image Data, *Physiology*, 2023, **38**, 5733149, DOI: **10.1152/physiol.2023.38.S1.5733149**.

43 D. W. Lee, N. Choi and J. H. Sung, A microfluidic chip with gravity-induced unidirectional flow for perfusion cell culture, *Biotechnol. Prog.*, 2019, **35**, e2701, DOI: **10.1002/btpr.2701**.

44 H.-T. Nguyen, S.-L. Rissanen, M. Peltokangas, T. Laakkonen, J. Kettunen, L. Barthod, R. Sivakumar, A. Palojärvi, P. Junttila, J. Talvitie, M. Bassis, S. L. Nickels, S. Kalvala, P. Ilina, P. Tammela, S. Lehtonen, J. C. Schwamborn, S. Mosser and P. Singh, Highly scalable and standardized organ-on-chip platform with TEER for biological barrier modeling, *Tissue Barriers*, 2024, 2315702, DOI: **10.1080/21688370.2024.2315702**.

45 B. Venzac, S. Deng, Z. Mahmoud, A. Lenferink, A. Costa, F. Bray, C. Otto, C. Rolando and S. Le Gac, PDMS Curing Inhibition on 3D-Printed Molds: Why? Also, How to Avoid It?, *Anal. Chem.*, 2021, **93**, 7180–7187, DOI: **10.1021/acs.analchem.0c04944**.

46 N. Limjanthong, Y. Tohbaru, T. Okamoto, R. Okajima, Y. Kusama, H. Kojima, A. Fujimura, T. Miyazaki, T. Kanamori, S. Sugiura and K. Ohnuma, Gravity-driven microfluidic device placed on a slow-tilting table enables constant unidirectional perfusion culture of human induced pluripotent stem cells, *J. Biosci. Bioeng.*, 2023, **135**, 151–159, DOI: **10.1016/j.jbiosc.2022.11.007**.

47 F. Minetti, A. Giorello, M. L. Olivares and C. L. A. Berli, Exact solution of the hydrodynamic focusing driven by hydrostatic pressure, *Microfluid. Nanofluid.*, 2020, **24**, 15, DOI: **10.1007/s10404-020-2322-y**.

48 A.-C. Vion, T. Perovic, C. Petit, I. Hollfinger, E. Bartels-Klein, E. Frampton, E. Gordon, L. Claesson-Welsh and H. Gerhardt, Endothelial Cell Orientation and Polarity Are Controlled by Shear Stress and VEGF Through Distinct Signaling Pathways, *Front. Physiol.*, 2021, **11**, 623769, DOI: **10.3389/fphys.2020.623769**.

49 C. A. Dessalles, C. Leclech, A. Castagnino and A. I. Barakat, Integration of substrate- and flow-derived stresses in endothelial cell mechanobiology, *Commun. Biol.*, 2021, **4**, 764, DOI: **10.1038/s42003-021-02285-w**.

50 P. Campinho, A. Vilfan and J. Vermot, Blood Flow Forces in Shaping the Vascular System: A Focus on Endothelial Cell Behavior, *Front. Physiol.*, 2020, **11**, 552, DOI: **10.3389/fphys.2020.00552**.

51 S. Dimmeler, B. Assmus, C. Hermann, J. Haendeler and A. M. Zeiher, Fluid shear stress stimulates phosphorylation of Akt in human endothelial cells: involvement in suppression of apoptosis, *Circ. Res.*, 1998, **83**, 334–341, DOI: **10.1161/01.res.83.3.334**.

52 L. Tai, Q. Zheng, S. Pan, Z.-G. Jin and B. C. Berk, Flow Activates ERK1/2 and Endothelial Nitric Oxide Synthase via a Pathway Involving PECAM1, SHP2, and Tie2, *J. Biol. Chem.*, 2005, **280**, 29620–29624, DOI: **10.1074/jbc.M501243200**.

53 T. Takahashi, A single autophosphorylation site on KDR/Flk-1 is essential for VEGF-A-dependent activation of PLC-gamma and DNA synthesis in vascular endothelial cells, *EMBO J.*, 2001, **20**, 2768–2778, DOI: **10.1093/emboj/20.11.2768**.

54 H. Jong Lee and G. Young Koh, Shear stress activates Tie2 receptor tyrosine kinase in human endothelial cells, *Biochem. Biophys. Res. Commun.*, 2003, **304**, 399–404, DOI: **10.1016/S0006-291X(03)00592-8**.

55 S. D. Castillo, E. Tzouanacou, M. Zaw-Thin, I. M. Berenjeno, V. E. R. Parker, I. Chivite, M. Milà-Guasch, W. Pearce, I. Solomon, A. Angulo-Urarte, A. M. Figueiredo, R. E. Dewhurst, R. G. Knox, G. R. Clark, C. L. Scudamore, A. Badar, T. L. Kalber, J. Foster, D. J. Stuckey, A. L. David, W. A. Phillips, M. F. Lythgoe, V. Wilson, R. K. Semple, N. J. Sebire, V. A. Kinsler, M. Graupera and B. Vanhaesebroeck, Somatic activating mutations in Pik3ca cause sporadic venous malformations in mice and humans, *Sci. Transl. Med.*, 2016, **8**(332), 332–343, DOI: **10.1126/scitranslmed.aad9982**.

56 N. Limaye, J. Kangas, A. Mendola, C. Godfraind, M. J. Schlögel, R. Helaers, L. Eklund, L. M. Boon and M. Vikkula, Somatic Activating PIK3CA Mutations Cause Venous Malformation, *Am. J. Hum. Genet.*, 2015, **97**, 914–921, DOI: **10.1016/j.ajhg.2015.11.011**.

57 S. Fukuhara, K. Sako, T. Minami, K. Noda, H. Z. Kim, T. Kodama, M. Shibuya, N. Takakura, G. Y. Koh and N. Mochizuki, Differential function of Tie2 at cell-cell contacts and cell-substratum contacts regulated by angiopoietin-1, *Nat. Cell Biol.*, 2008, **10**, 513–526, DOI: **10.1038/ncb1714**.

58 M.-J. Yoon, C.-H. Cho, C. S. Lee, I.-H. Jang, S. H. Ryu and G. Y. Koh, Localization of Tie2 and phospholipase D in endothelial caveolae is involved in angiopoietin-1-induced MEK/ERK phosphorylation and migration in endothelial cells, *Biochem. Biophys. Res. Commun.*, 2003, **308**, 101–105, DOI: **10.1016/S0006-291X(03)01341-X**.

59 R. Pietilä, M. Nätynki, T. Tammela, J. Kangas, K. H. Pulkki, N. Limaye, M. Vikkula, G. Y. Koh, P. Saharinen, K. Alitalo and L. Eklund, Ligand oligomerization state controls Tie2 receptor trafficking and angiopoietin-2-specific responses, *J. Cell Sci.*, 2012, jcs.098020, DOI: **10.1242/jcs.098020**.

60 P. Saharinen, L. Eklund, J. Miettinen, R. Wirkkala, A. Anisimov, M. Winderlich, A. Nottebaum, D. Vestweber, U. Deutsch, G. Y. Koh, B. R. Olsen and K. Alitalo, Angiopoietins assemble distinct Tie2 signalling complexes in endothelial cell-cell and cell-matrix contacts, *Nat. Cell Biol.*, 2008, **10**, 527–537, DOI: **10.1038/ncb1715**.

61 B. Melchior and J. A. Frangos, Distinctive subcellular Akt-1 responses to shear stress in endothelial cells, *J. Cell. Biochem.*, 2014, **115**, 121–129, DOI: **10.1002/jcb.24639**.

62 T. Kaur, R. Kapila and S. Kapila, MicroRNAs as Next Generation Therapeutics in Osteoporosis, *Clin. Implementation Bone Regener. Maint.*, 2021, DOI: **10.5772/intechopen.91223**.

63 N. Li-Villarreal, R. L. Y. Wong, M. D. Garcia, R. S. Udan, R. A. Poché, T. L. Rasmussen, A. M. Rhyner, J. D. Wythe and M. E. Dickinson, FOXO1 represses sprouty 2 and sprouty 4 expression to promote arterial specification and vascular remodeling in the mouse yolk sac, *Development*, 2022, **149**, dev200131, DOI: **10.1242/dev.200131**.

64 I. Xanthis, C. Souilhol, J. Serbanovic-Canic, H. Roddie, A. C. Kalli, M. Fragiadaki, R. Wong, D. R. Shah, J. A. Askari, L. Canham, N. Akhtar, S. Feng, V. Ridger, J. Waltho, E. Pinteaux, M. J. Humphries, M. T. Bryan and P. C. Evans, β1 integrin is a sensor of blood flow direction, *J. Cell Sci.*, 2019, **132**, jcs229542, DOI: **10.1242/jcs.229542**.

65 M. Lindner, A. Laporte, L. Elomaa, C. Lee-Thedieck, R. Olmer and M. Weinhart, Flow-induced glycocalyx formation and cell alignment of HUVECs compared to iPSC-derived ECs for tissue engineering applications, *Front. Cell. Dev. Biol.*, 2022, **10**, 953062, DOI: **10.3389/fcell.2022.953062**.

66 H.-W. Lee, J. H. Shin and M. Simons, Flow goes forward and cells step backward: endothelial migration, *Exp. Mol. Med.*, 2022, **54**, 711–719, DOI: **10.1038/s12276-022-00785-1**.

67 H. Park, J. Furtado, M. Poulet, M. Chung, S. Yun, S. Lee, W. C. Sessa, C. A. Franco, M. A. Schwartz and A. Eichmann, Defective Flow-Migration Coupling Causes Arteriovenous Malformations in Hereditary Hemorrhagic TelangiectasiaHyojin, *Circulation*, 2021, **144**(10), 805–822, DOI: **10.1161/CIRCULATIONAHA.120.053047**.

68 S. Chlench, N. Mecha Disassa, M. Hohberg, C. Hoffmann, T. Pohlkamp, G. Beyer, M. Bongrazio, L. Da Silva-Azevedo, O. Baum, A. R. Pries and A. Zakrzewicz, Regulation of Foxo-1 and the angiopoietin-2/Tie2 system by shear stress, *FEBS Lett.*, 2007, **581**, 673–680, DOI: **10.1016/j.febslet.2007.01.028**.